

Brain tumor classification using the diffusion tensor image segmentation (D-SEG) technique

Timothy L. Jones, Tiernan J. Byrnes, Guang Yang, Franklyn A. Howe, B. Anthony Bell, and Thomas R. Barrick

Academic Neurosurgery Unit, St. Georges, University of London, London, UK (T.L.J., T.J.B., B.A.B.); Neurosciences Research Centre, Cardio-vascular and Cell Sciences Institute, St. George's, University of London, London, UK (G.Y., F.A.H., T.R.B.)

Corresponding Author: Timothy L. Jones, PhD, Academic Neurosurgery Unit, St George's, University of London, Cranmer Terrace, London, SW17 0RE, UK (drtimjones@hotmail.com).

Background. There is an increasing demand for noninvasive brain tumor biomarkers to guide surgery and subsequent oncotherapy. We present a novel whole-brain diffusion tensor imaging (DTI) segmentation (D-SEG) to delineate tumor volumes of interest (VOIs) for subsequent classification of tumor type. D-SEG uses isotropic (p) and anisotropic (q) components of the diffusion tensor to segment regions with similar diffusion characteristics.

Methods. DTI scans were acquired from 95 patients with low- and high-grade glioma, metastases, and meningioma and from 29 healthy subjects. D-SEG uses k -means clustering of the 2D (p, q) space to generate segments with different isotropic and anisotropic diffusion characteristics.

Results. Our results are visualized using a novel RGB color scheme incorporating p , q and T2-weighted information within each segment. The volumetric contribution of each segment to gray matter, white matter, and cerebrospinal fluid spaces was used to generate healthy tissue D-SEG spectra. Tumor VOIs were extracted using a semiautomated flood-filling technique and D-SEG spectra were computed within the VOI. Classification of tumor type using D-SEG spectra was performed using support vector machines. D-SEG was computationally fast and stable and delineated regions of healthy tissue from tumor and edema. D-SEG spectra were consistent for each tumor type, with constituent diffusion characteristics potentially reflecting regional differences in tissue microstructure. Support vector machines classified tumor type with an overall accuracy of 94.7%, providing better classification than previously reported.

Conclusions. D-SEG presents a user-friendly, semiautomated biomarker that may provide a valuable adjunct in noninvasive brain tumor diagnosis and treatment planning.

Keywords: biomarker, brain tumor, diffusion tensor imaging, glioblastoma, segmentation.

The imaging characteristics of newly identified brain tumors may indicate the likely diagnosis and treatment strategy. Until recently, certain cases of malignant glioma (glioblastoma) and metastatic brain tumors were often considered untreatable.^{1,2} Advances in chemotherapeutic and radiotherapy regimens³ and appreciation of the role of surgical resection in survival⁴ resulted in more patients being recommended for treatment. Histological confirmation is usually necessary prior to commencing therapy, yet there remain risks associated with surgery.⁵ Noninvasive, accurate, and reproducible biomarkers are required to assist with decision making.

Typical “preoperative” tumor MR protocols include T2-weighted, diffusion-weighted, and gadolinium enhanced T1-weighted imaging to evaluate lesion cellularity, vascularity, and blood–brain barrier integrity. These “conventional”

sequences yield a correct diagnosis in the majority of cases. However, there remains a lack of specificity in challenging scenarios, such as differentiating: (i) malignant (World Health Organization [WHO] grades III and IV) glial tumors from low-grade glioma (WHO grades I and II),⁶ (ii) malignant glioma from solitary necrotic or cystic cerebral metastasis,⁷ and (iii) benign en-plaque meningeal tumors (eg, meningioma) from durally based metastatic deposits.⁸

Quantifying microscopic diffusion of water molecules using MRI is a proposed surrogate marker of tissue microstructure.⁹ Brain tumors alter regional brain architecture due to differences in cell structure, size, and density and the presence of necrosis and edema. Consequently, tumor MR diffusion properties may identify diagnostic intertumoral differences. Whole-brain maps of diffusion metrics can be

Received 25 February 2014; accepted 7 July 2014

© The Author(s) 2014. Published by Oxford University Press on behalf of the Society for Neuro-Oncology.

This is an Open Access article distributed under the terms of the Creative Commons Attribution Non-Commercial License (<http://creativecommons.org/licenses/by-nc/4.0/>), which permits non-commercial re-use, distribution, and reproduction in any medium, provided the original work is properly cited. For commercial re-use, please contact journals.permissions@oup.com

generated from diffusion tensor imaging (DTI) data.^{10,11} Mean diffusivity (MD) provides a magnitude of isotropic diffusion (in $\text{mm}^2 \text{s}^{-1}$), and fractional anisotropy (FA) provides a scalar value of diffusion directionality. Differences in MD and FA among tumor types and grades of malignancy have been investigated with mixed success.¹²⁻¹⁶

An alternative decomposition of the diffusion tensor is into isotropic (p) and anisotropic (q) components,¹⁷ where p is a scaled measure of MD, and q is a measure of deviation of the principal diffusivities from isotropy, both in units of $\text{mm}^2 \text{s}^{-1}$:

$$p = \sqrt{3}MD \quad (1)$$

$$q = \sqrt{(\lambda_1 - MD)^2 + (\lambda_2 - MD)^2 + (\lambda_3 - MD)^2} \quad (2)$$

where λ_1 , λ_2 , and λ_3 are the principal diffusivities of the diffusion tensor and $MD = (\lambda_1 + \lambda_2 + \lambda_3)/3$. Each image voxel from a DTI dataset can be represented as a coordinate in a 2D Cartesian plane referred to as (p,q) space.

The majority of studies investigating DTI metrics in tumor diagnosis utilize manually determined regions of interest (ROIs) subjectively placed within tumor regions (eg, solid/necrotic tumor component, normal-appearing brain, perilesional tissue). ROI placement guided by intensity boundaries on conventional MR images is generally performed on a single image slice, yielding an ROI smaller than the entire lesion.

Automated lesion segmentation is an alternative ROI selection technique¹⁸ but has been applied mostly to conventional MRI,¹⁹⁻²² with few examples of tumor segmentation from diffusion-weighted imaging (DWI) or DTI datasets.^{23,24} Ideally, tumor segmentation requires minimal user input, is computationally efficient, and classifies images into regions with different pathological microstructures. In whole-brain DTI datasets, this corresponds to segmenting regions sharing similar diffusion characteristics to reflect similar tissue microstructure.

We present a novel diffusion segmentation (D-SEG) algorithm applied to (p,q) space. D-SEG automatically segments and visualizes regions of similar diffusion characteristics. Pattern recognition by k -means clustering²⁵ is used to iteratively segment (p,q) space into K nonoverlapping clusters. The number, K , of initial centroids is specified a priori according to the number of desired clusters²⁶ as determined by functional and anatomical considerations. Tumor tissue boundaries identified on D-SEG maps are used to semiautomatically delineate volumes of interest (VOIs). The relative proportion of each (p,q) segment within the VOI reflects the composition of isotropic and anisotropic diffusion within the lesion, providing a “signature” referred to as a D-SEG spectrum. D-SEG is applied to a cohort of young healthy subjects and a large cohort of tumor patients to investigate lesion-specific diffusion signatures as surrogate markers of tumor microstructure. Classification of D-SEG spectra into tumor types is then performed using support vector machines (SVMs).

Materials and Methods

Patients

All patients participating in this study signed a consent form approved by the research ethics committee. Ninety-five patients

(mean age 56.3 ± 16.1 y) and 29 healthy subjects (mean age 27.4 ± 7.3 y) were prospectively recruited over an 18-month period. Patient inclusion criteria were: a radiologically diagnosed lesion occupying intracranial space due to undergo surgery with subsequent histopathological confirmation of tumor type; age over 16 years; and ability to lie flat for ~ 1 h. Tumor types were: 11 WHO grade I meningiomas, 26 metastases, 31 solid grade IV glioblastomas, 7 cystic grade IV glioblastomas, 1 grade III anaplastic astrocytoma, and 19 grade II low-grade gliomas. Of the 95 patients, 82 underwent lesion debulking/resection (11 meningiomas, 26 metastases, 28 high grade gliomas, 16 low-grade gliomas) and 13 had a stereotactic biopsy (10 grade IV glioblastomas, 3 low-grade gliomas). All cases of glioblastoma displayed contrast enhancement on T1-weighted imaging, and of the 19 cases of low-grade glioma, 16 did not enhance and 3 displayed a faint blush of enhancement. Targeted biopsy of the enhancing region in the low-grade glioma patients did not reveal focal cellular anaplasia. Of the 26 metastases studied, 10 originated from lung carcinoma, 7 from breast carcinoma, 3 melanoma, 3 renal, 2 bowel adenocarcinoma, and 1 prostate. Tumors were all intra-axial and supratentorial; 14 were solitary and 12 were multiple lesions.

Image Acquisition

DTIs were acquired using 2 similar 1.5T scanners (termed A and B). Although scanner acquisitions differed, echo times (TEs) were similar, and repetition times (TRs) were long enough to avoid T1-relaxation effects. Voxel sizes and DTI signal to noise were similar on each scanner due to acquisition of 12 and 61 diffusion gradient directions, with 4 and 1 average(s), respectively. Whole-brain coverage was achievable in a single acquisition using scanner B, reducing total acquisition time.

Scanner A

MRIs were acquired for 41 patients (6 meningiomas, 11 metastases, 13 glioblastomas, 11 grade II gliomas) and 16 young healthy subjects (1.5T General Electric Signa LX, quadrature head coil, maximum gradient strength 22 mT m^{-1}). Axial DTIs were acquired using a single-shot spin echo planar imaging (EPI) sequence. Following acquisition at $b = 0 \text{ s mm}^{-2}$ (repeated 10 times), DWIs were acquired ($b = 1000 \text{ s mm}^{-2}$) with diffusion gradients applied in 12 directions (TE, 88 ms; TR, 8000 ms; field of view = $240 \times 240 \text{ mm}^2$; matrix size = 96×96 ; slice gap, 2.8 mm; slice thickness, 2.8 mm), providing near isotropic voxels $2.5 \times 2.5 \times 2.8 \text{ mm}^3$. Two interleaved acquisitions were acquired, providing contiguous whole-brain coverage over 50 slices and repeated 4 times to improve signal to noise. The T2-weighted EPI $b = 0 \text{ s mm}^{-2}$ images are subsequently referred to as $b = 0$ maps.

Scanner B

MRIs were acquired for 54 patients (5 meningiomas, 15 metastases, 25 glioblastomas, 1 anaplastic astrocytoma, and 8 grade II gliomas) and 13 young healthy subjects (1.5T GE Signa HDx, 8-channel head coil, maximum gradient strength 33 mT m^{-1}). Differences in DTI acquisition on scanner B compared with scanner A were that whole-brain DWIs were acquired at a

higher angular resolution in 61 noncollinear diffusion gradient directions (TE, 94 ms; TR, 14 000 ms; slice thickness, 2.5 mm; no slice gap), providing 2.5 mm isotropic voxels over 55 slices.

Image Preprocessing

DWIs were realigned to remove eddy current distortions using eddy correct (FMRIB Software Library, <http://www.fmrib.ox.ac.uk/fsl>) prior to generating p and q maps. Images were skull stripped using Brain Extraction Tool (FMRIB Software).

Reproducibility of DTI Data Between Scanners

Between-scanner reproducibility was estimated with 5 healthy subjects. For each subject, $b = 0$ maps acquired on scanner B were coregistered to those obtained on scanner A using an affine transformation (Statistical Parametric Mapping [SPM]8, <http://www.fil.ion.ucl.ac.uk/SPM8>) and were used to coregister p and q maps. Tissue probability maps of gray matter (GM), white matter (WM), and CSF were computed from each $b = 0$ map SPM8.²⁷ Hard segmentation maps were computed for GM, WM, and CSF (eg, for GM, $p(\text{GM}) > p(\text{WM}) + p(\text{CSF})$ at each voxel). Voxel-wise comparison of p and q values yielded intra-class correlation coefficients for GM and WM.

DTI Segmentation Algorithm

Histograms of p and q were computed across all brain voxels in all subjects ($n = 123$). High intensity noise was removed from the p and q distributions by computing 99.99 percentiles and assigning values above this threshold to 1.0. Remaining voxels were scaled between 0 and 1, generating dataset-wide non-Gaussian p and q histograms (Fig. 1A and B).

The p and q maps are a set of observations (x_1, x_2, \dots, x_n) where each observation is a 2D real vector in (p, q) space (Fig. 1C). Clustering by k -means partitions the n data points into K disjoint subsets S_j , where $j = \{1, 2, \dots, 16\}$ by minimizing the within-cluster sum of squares objective function,

$$J = \sum_{j=1}^K \sum_{n \in S_j} \|x_n - \mu_j\|^2,$$

where x_n is a vector representing the n th data point, and μ_j is the geometric centroid of the data points in S_j . Centroids of the initial clusters ($\mu_1, \mu_2, \dots, \mu_n$) were selected by separating (p, q) space into K segments of roughly equal size according to median and quartile values of p and q (Fig. 1D, Table 1). These initial conditions preserve the non-Gaussian structure of the p and q histograms in the cluster initialization. As the data are non-Gaussian, the centroid was defined to be the median (p, q) coordinate of each cluster. The following 2 steps of the algorithm²⁵ were repeated:

Step 1. Assignment step: Assign each voxel to the cluster whose centroid is closest in (p, q) space, thus partitioning the voxels into K clusters, shown here at the t th iteration,

$$S_i^{(t)} = \{x_j : \|x_j - \mu_i^{(t)}\| \leq \|x_j - \mu_{i^*}^{(t)}\| \text{ for all } i^*, i \in \{1, \dots, K\}\}.$$

Step 2. Update step: Calculate the new centroids for each

cluster, shown for iteration $t + 1$,

$$\mu_i^{(t+1)} = \frac{1}{|S_i^{(t)}|} \sum_{x_j \in S_i^{(t)}} x_j.$$

An iterative exponential decrease in the number of voxels changing cluster was observed. D-SEG was terminated after 250 iterations, after which convergence was achieved. Final segmentation of (p, q) space is displayed as a Voronoi tessellation²⁸ (Fig. 1E).

Selection of K

We tested our segmentation technique using a range of different K values ($K = 4, 9, 16$, and 25). $K = 16$ was selected because it provided the optimum computation time and allowed identification of our a priori postulated regions within a tumor-affected brain, namely: (i) healthy brain GM, (ii) heterogeneous WM, (iii) CSF, (iv) solid tumor, (v) regional necrosis, (vi) tumor-associated cystic regions, (vii) perilesional edema, (viii) perilesional tumor infiltration, and (ix) distant edema while also identifying differences among the 5 tumor types studied.

D-SEG Color Visualization Technique

A novel RGB coloring scheme was developed to illustrate the relative magnitude of p and q diffusion and T2-weighting (from the $b = 0$ map) within each D-SEG cluster. A histogram of T2-weighted intensities was computed for each subject, the 99.99 percentile was discarded, and resultant values were scaled between 0 and 1. Median p , q , and T2-weighted values for cluster centroids were ranked from 1 (lowest median) to 16 (highest median). Rank scores were used to generate an RGB color by assigning T2-weighting, p , and q to the red, green, and blue channels, respectively (Fig. 2). Color maps were visualized using MRICro.²⁹

D-SEG in Healthy Subjects

Hard segmentation of $b = 0$ maps into GM, WM, and CSF was computed using SPM8 as described above to mask each of the D-SEG maps. The proportion of each segment within each tissue type was determined and plotted to provide average D-SEG spectra across all healthy subjects.

Tumor and Edema Volume of Interest Delineation

A combined tumor and edema VOI was semiautomatically delineated for each patient using a 4-voxel neighborhood recursive flood-filling algorithm on a slice-by-slice basis. Seed voxel(s) were placed within tumor and edema by a neurosurgeon (T.J.) with 6 years of training and 4 years of clinical and research experience of lesion delineation. T.J. was blinded to the histopathological diagnosis, and the semiautomated segmentation was performed directly from the D-SEG maps with conventional T2-weighted and T1-weighted images (+/- contrast) as additional visual guides. No manual editing of the VOI was performed post hoc.

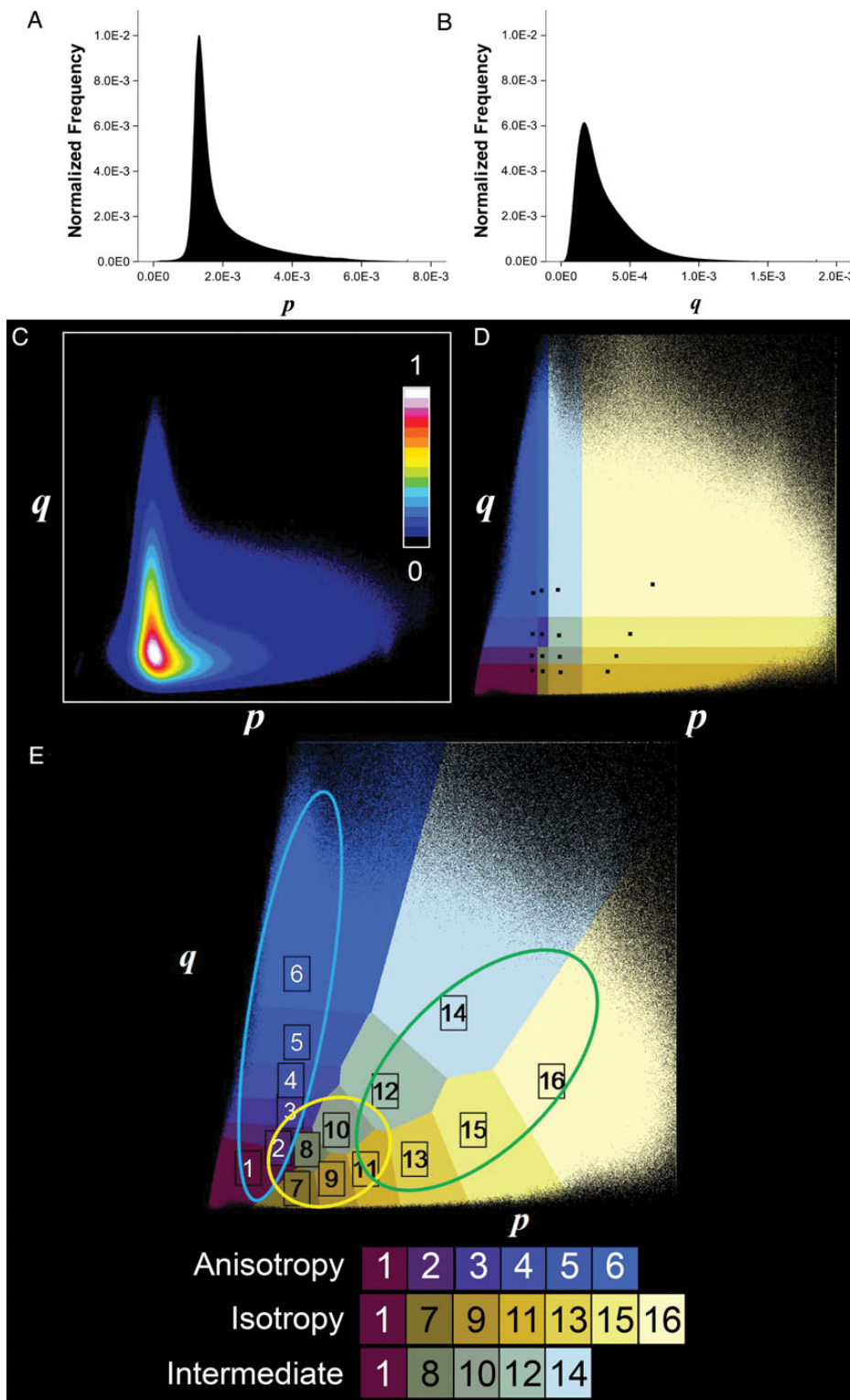


Fig. 1. D-SEG clustering technique. Normalized histograms of (A) p and (B) q across all subjects ($n = 123$). (C) The normalized 2D histogram in (p,q) space for all subjects. (D) Initial clusters with medians in (p,q) space. (E) Voronoi plot of final clusters (after 250 iterations of the k -means algorithm). All clusters are colored using the D-SEG color mapping technique after 250 iterations (Fig. 2). Cluster numbers in (E) were assigned based on median rank of p in each cluster. Specific segments are associated with increasing anisotropic diffusivity (1 to 6), increasing isotropic diffusivity (1, 7, 9, 11, 13, 15, and 16), and increasing intermediate diffusivity (1, 8, 10, 12, and 14). Ellipses in (E) show the (p,q) range of healthy tissue diffusivities (blue = WM, yellow = GM, green = CSF).

Table 1. Number and percent of voxels in each D-SEG segment at initialization and termination of the *k*-means algorithm

| Segment Number | Initial Conditions | | Algorithm Termination (250 iterations) | | | |
|----------------|------------------------------|-----------------|--|-----------------|--|--|
| | Number of Constituent Voxels | Total Voxels, % | Number of Constituent Voxels | Total Voxels, % | p ($\text{mm}^2 \text{s}^{-1} \times 10^{-3}$) | q ($\text{mm}^2 \text{s}^{-1} \times 10^{-4}$) |
| 1 | 4116043 | 4.66 | 9732194 | 11.01 | 1.22 | 1.85 |
| 2 | 5720616 | 6.47 | 9102275 | 10.30 | 1.30 | 2.86 |
| 3 | 6380942 | 7.22 | 6440093 | 7.29 | 1.32 | 3.85 |
| 4 | 5870246 | 6.64 | 4277553 | 4.84 | 1.34 | 5.00 |
| 5 | 5260481 | 5.95 | 9109123 | 10.31 | 1.36 | 6.59 |
| 6 | 5478436 | 6.20 | 7865938 | 8.90 | 1.45 | 9.41 |
| 7 | 5628352 | 6.37 | 7741129 | 8.76 | 1.45 | 1.19 |
| 8 | 5720574 | 6.47 | 2124115 | 2.40 | 1.57 | 2.11 |
| 9 | 8059367 | 9.12 | 7155477 | 8.10 | 1.94 | 1.40 |
| 10 | 6044389 | 6.84 | 4351102 | 4.92 | 2.03 | 3.14 |
| 11 | 4416182 | 5.00 | 3426063 | 3.88 | 2.54 | 1.73 |
| 12 | 3567915 | 4.04 | 1956397 | 2.21 | 2.79 | 4.68 |
| 13 | 4651951 | 5.27 | 5434604 | 6.15 | 3.26 | 2.05 |
| 14 | 4844407 | 5.48 | 4128078 | 4.67 | 3.85 | 7.73 |
| 15 | 5662375 | 6.41 | 3329037 | 3.77 | 4.20 | 3.03 |
| 16 | 6929118 | 7.84 | 2178216 | 2.47 | 5.48 | 4.96 |

Median coordinates in (p,q) space quantify diffusion characteristics for each segment.

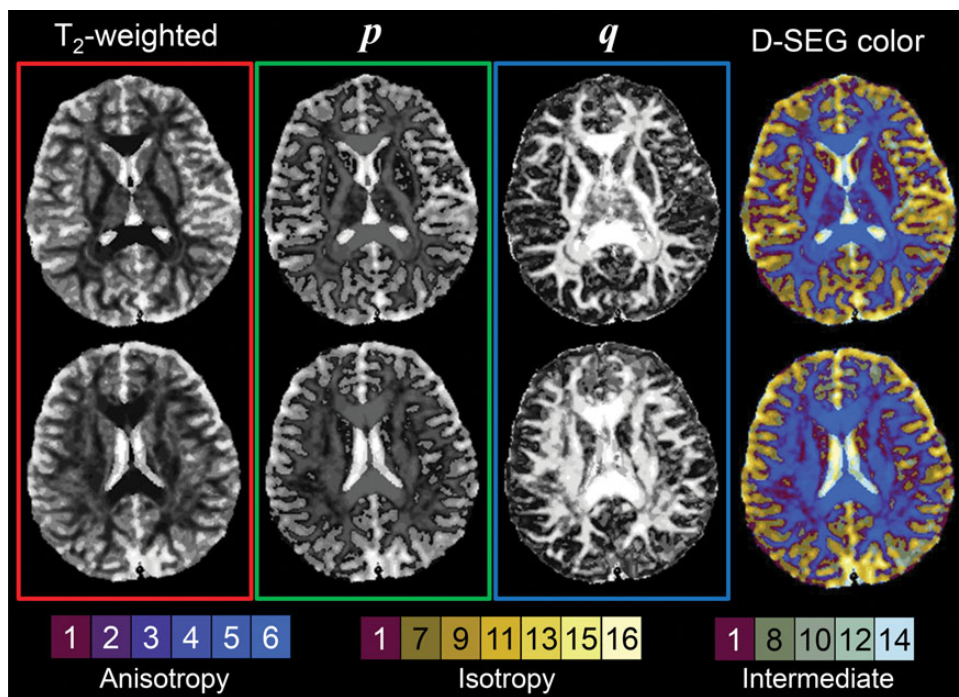


Fig. 2. D-SEG color mapping technique. Ranked T2-weighted (red channel), p (green channel), and q (blue channel) maps are shown to the left of D-SEG color maps for 2 axial slices of a healthy subject.

D-SEG Tumor Spectra

The volumetric proportion of each (p,q) segment to the VOI was calculated for each case and averaged across tumor type to generate D-SEG tumor spectra for low-grade glioma,

glioblastoma multiforme (GBM), cystic GBM, metastases, and meningioma. Group spectra and classification were not performed for the anaplastic astrocytoma case due to insufficient group size ($n = 1$).

Table 2. Cross-validated diagnostic results ($n = 94$), SVM analysis of D-SEG spectra

| Tumor Type | LGG | GBM | cGBM | MET | MEN | Total | Sens. | Spec. | Accu. | 95% CI | BER |
|---|-----|-----|------|-----|-----|-------|-------|-------|-------|-------------|-----|
| A Confusion matrix—61 direction DTI | | | | | | | | | | | |
| LGG | 10 | 0 | 0 | 0 | 1 | 11 | 90.9 | 97.5 | 96.1 | (86.5–99.5) | |
| GBM | 0 | 14 | 0 | 0 | 0 | 14 | 100 | 100 | | | |
| cGBM | 0 | 0 | 6 | 0 | 0 | 6 | 100 | 100 | | | |
| MET | 0 | 0 | 0 | 16 | 0 | 16 | 100 | 100 | | | |
| MEN | 1 | 0 | 0 | 0 | 3 | 4 | 75 | 97.9 | | | |
| B Confusion matrix—12 direction DTI | | | | | | | | | | | |
| LGG | 7 | 0 | 0 | 0 | 1 | 8 | 87.5 | 100 | 93.0 | (80.9–98.5) | |
| GBM | 0 | 17 | 0 | 0 | 0 | 17 | 100 | 96.2 | | | |
| cGBM | 0 | 0 | 1 | 0 | 0 | 1 | 100 | 100 | | | |
| MET | 0 | 1 | 0 | 9 | 0 | 10 | 90 | 97.2 | | | |
| MEN | 0 | 0 | 0 | 1 | 6 | 7 | 85.7 | 97.2 | | | |
| C Confusion matrix—combined datasets | | | | | | | | | | | |
| LGG | 19 | 0 | 0 | 0 | 0 | 19 | 100.0 | 97.3 | 94.7 | (88.0–98.3) | 6.9 |
| GBM | 0 | 30 | 1 | 0 | 0 | 31 | 96.8 | 98.4 | | | |
| cGBM | 0 | 1 | 6 | 0 | 0 | 7 | 85.7 | 98.9 | | | |
| MET | 2 | 0 | 0 | 24 | 0 | 26 | 92.3 | 98.5 | | | |
| MEN | 0 | 0 | 0 | 1 | 10 | 11 | 90.9 | 100.0 | | | |

Abbreviations: cGBM, cystic GBM; LGG, low-grade glioma; MEN, meningioma; MET, metastasis. Sens., sensitivity (%); Spec., specificity (%); Accu., accuracy (%); BER, balanced error rate (%).

Tumor Classification

The ability of D-SEG spectra to classify tumor type was tested across all patients using SVMs.³⁰ SVM predictions depend on only a subset of the training data (ie, the support vectors). The technique finds the hyperplane with the largest margin of difference between classes.³¹ We used the Gaussian radial basis function kernel ($\sigma = 1$) to map feature vectors into a non-linear feature space where an optimal hyperplane was constructed separating tumor classes. Tenfold cross-validation was used to test classification accuracy and reproducibility. To test the integrity of combining tumor DTI from 2 different scanners, separate SVM classifications of D-SEG spectra acquired for each acquisition protocol were performed (Table 2A and B).

Results

Between-Scanner Reproducibility

Mean and standard deviation for intraclass correlation coefficients for GM (0.915 ± 0.097) and WM (0.890 ± 0.110) in healthy volunteers showed good interscanner reproducibility of p and q diffusion metrics for healthy tissue.

D-SEG Algorithm

The D-SEG algorithm was computationally fast and reached steady state by 50 iterations. Non-Gaussian characteristics were apparent in p and q histograms (Fig. 1A and B) and in the histogram of (p,q) space. The initial 16 segments assigned to the (p,q) distribution and the final segmentation after 250 iterations are shown in Fig. 1D and E. Table 1 provides the initial and final numbers of voxels in each segment and their median

(p,q) coordinates. The Voronoi plot (Fig. 1E) shows 3 radial lines of segments through (p,q) space with unique diffusion characteristics that include: tissue with mostly anisotropic diffusivity (with q increasing from segment 1 to 6) but with lowest isotropic diffusivity, isotropic diffusivity (with p increasing from segment 1 through 7, 9, 11, 13, 15, and 16), and intermediate diffusivity (with p and q increasing from segment 1 through 8 and 12 to 14).

D-SEG Color Mapping

D-SEG color mapping is shown in Fig. 2 for a healthy subject. The color mapping technique provides visually distinct colors based on the diffusion and T2-weighted properties of the tissue in each voxel. White matter regions with high anisotropic diffusion are colored blue. Gray matter regions with low anisotropic and isotropic diffusivities are yellow-brown with CSF colored pale yellow.

D-SEG Spectra in Healthy Subjects

Gray matter, WM, and CSF voxels occupy different regions of (p,q) space, as shown schematically by the ellipses in Fig. 1E, and proportionately include different segment amounts resulting in characteristic D-SEG tissue spectra (Fig. 4A). Gray matter predominantly includes segments 1, 2, 7, 8, and 9, representing low isotropic and anisotropic diffusivities, whereas WM almost exclusively includes segments 1 to 6, representing low isotropic diffusion and increasing levels of anisotropic diffusion. CSF spaces include high isotropic diffusion characteristics (segments 14, 15, and 16). Tissue partial volume effects will be present in D-SEG segments because tissue class was not used to define the segmentation.

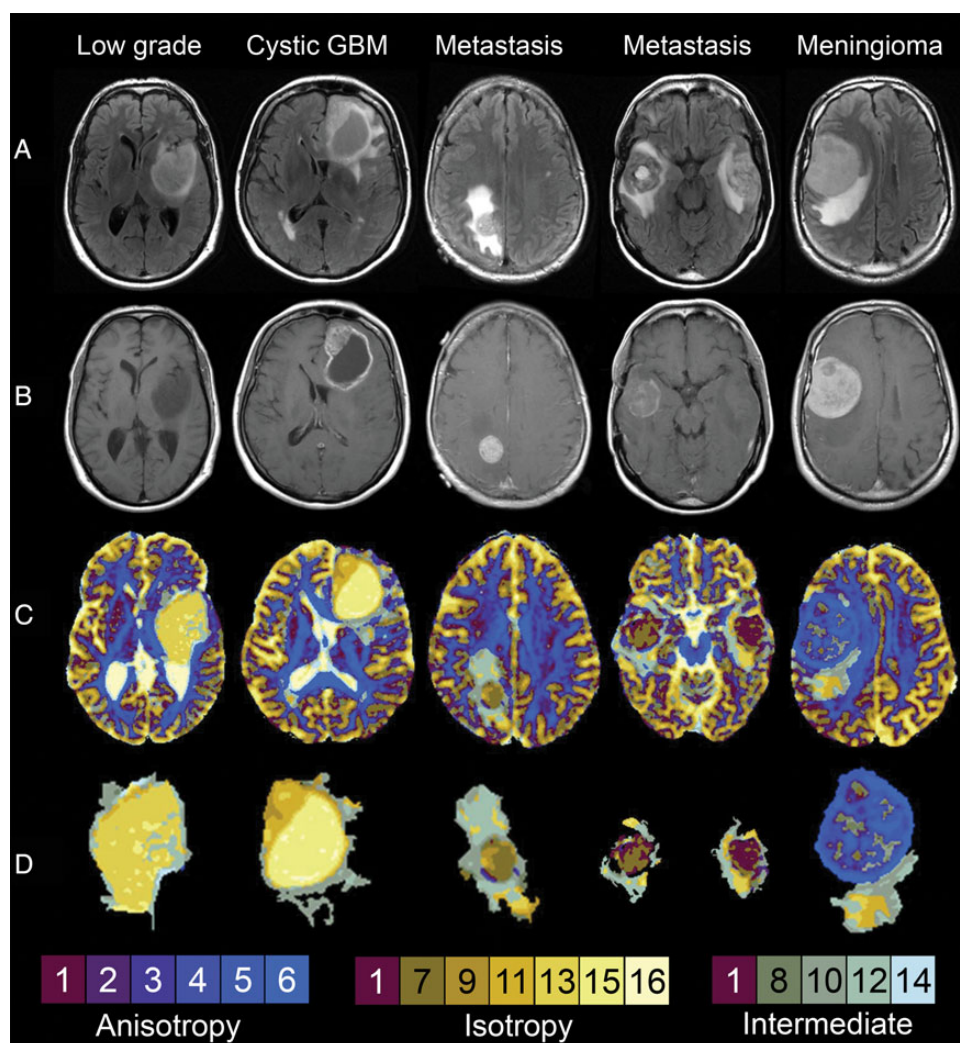


Fig. 3. Individual patient images. From left to right: grade II glioma, glioblastoma with cystic component, cerebral metastasis, and meningioma examples. (A) Fluid attenuated inversion recovery images, (B) T1-weighted postcontrast images, (C) D-SEG color maps, and (d) tumor volumes of interest. All images are illustrated using the radiological convention.

Tumor Volume of Interest Delineation

Examples of the VOI extraction technique are shown in Fig. 3 for low-grade glioma, glioblastoma, metastases, and meningioma. Conventional fluid attenuated inversion recovery (row A) and postcontrast T1-weighted images (row B) indicate the tumor core, cystic, and edematous regions. D-SEG color maps show the isotropic and anisotropic diffusion characteristics of the tumor cases (row C) with the extracted VOIs (row D). D-SEG color images show a visually apparent boundary between healthy and abnormal tissue (solid tumor, necrosis, cyst, and edema) that relates to differences in diffusion characteristics located in the regions identified as abnormal in the conventional images. While lesion margins on conventional MRI can be visually indistinct and rely on a subjective choice of thresholding level, the colored segments obtained by D-SEG provide a more objective boundary for semiautomatic lesion delineation.

Tumor D-SEG Spectra

Figure 4B–F illustrates average D-SEG spectra obtained within the VOIs for each tumor type. The low-grade glioma spectrum consisted mostly of segments 9, 11, and 13, representing a lower anisotropic and higher isotropic diffusion relative to healthy WM. High proportions of intermediate diffusivity segments 10 and 12 potentially represent partial volume effects between tumor and WM tissue and were located at the tumor boundary. The glioblastoma spectrum contained segments of low anisotropic and isotropic diffusivity (segments 7 and 9, likely corresponding to solid tumor) as well as segments with high isotropic and low anisotropic diffusivity (segments 12 and 13, likely corresponding to necrotic regions). High proportions of segments 8, 10, and 11 with greater isotropic diffusivities potentially represent edema regions. Cystic glioblastoma spectra shared such diffusion characteristics but with high proportions of segment 15 corresponding to the cystic region. The D-SEG spectrum of metastases contains

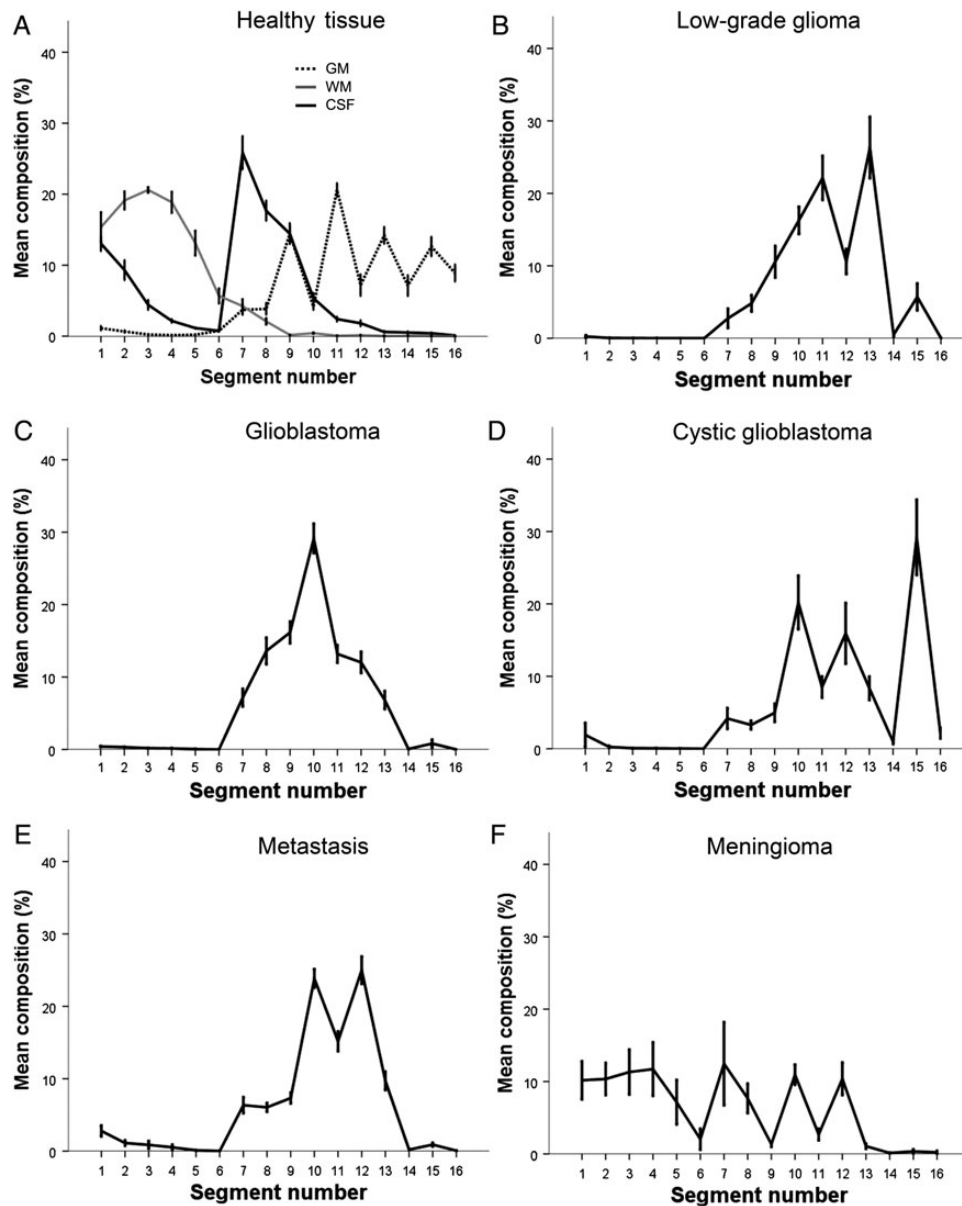


Fig. 4. D-SEG spectra. Average proportion of D-SEG segments within VOIs (standard error shown) for: (A) healthy tissue, (B) grade II glioma, (C) glioblastoma, (D) glioblastoma with cystic component, (E) cerebral metastasis, and (F) meningioma.

segments 1, 7, 8, and 9 (low isotropic and low anisotropic diffusivity), corresponding to the solid tumor component. Segments 10 and 12 likely represent perilesional edema with isotropic diffusivities greater than for glioblastoma. The D-SEG meningioma spectrum is markedly different from the other tumor types, with a large contribution from segments 1, 2, 3, and 4 (low isotropic and increasing anisotropic diffusion), representing the solid tumor component. In common with the metastases spectrum, segments 10 and 12 represent the edema region.

Classification of Tumor Type

SVM analysis of the D-SEG spectra classified tumor type with high overall accuracy (95% CI: 88.0%–98.3%) and low

balanced error rate of 6.9% after cross-validation (Table 2C). Sensitivity and specificity of tumor classification was >90% and 97%, respectively, for all tumor types except cystic glioblastoma. Separate SVM analysis of tumor spectra from the different DTI acquisitions reveals comparable accuracies (96.1% CI: 86.5%–99.5% for 61-direction DTI vs 93.0% CI: 80.9%–98.5% for 12-direction DTI; Table 2A and B).

Discussion

We present D-SEG, a fast segmentation and visualization technique that employs k -means clustering of (p, q) space to provide tissue segments with different isotropic and anisotropic diffusion properties. D-SEG maps were colored according to ranked

T2-weighted, p and q segment median values to provide a simple visualization of diffusion characteristics throughout the entire brain that was then used to semiautomatically extract VOIs of abnormal tissue. Distinct D-SEG tumor spectra representing the proportion of diffusion segments within the VOI were computed, and SVMs provided exceptionally high classification accuracy among brain tumor types and grades.

Difficulties arise in multicenter studies incorporating MR diffusion metrics due to variability in scanner magnetic field, gradient strength, coil channels, and acquisition protocols.³² Despite the use of two 1.5T MR scanners with different maximum gradient strengths and acquisition protocols, the inter-scanner reproducibility of p and q metrics was comparable to previous studies.^{33,34} This led to consistent D-SEG spectral patterns in healthy tissue and tumor VOIs for data acquired from 2 MR systems. A separate SVM subanalysis of tumor VOI D-SEG spectra generated from the 2 different DTI acquisitions revealed comparable diagnostic accuracies, confirming that the datasets may be combined for the presented analysis.

The D-SEG technique separates (p, q) space into segments with distinct isotropic and anisotropic diffusion properties. Simultaneous application of D-SEG to all healthy and patient data ensured that segments contained voxels with the same diffusion properties in each individual. This allowed meaningful between-subject comparison of D-SEG spectra. Nevertheless, further work is required to evaluate stability of the final D-SEG result due to perturbation of the initial algorithmic conditions and for different numbers of tumor datasets. In this study, initial conditions were chosen that reflected the local density of (p, q) space and consequently provided similar voxel numbers per segment. Alternative segmentation techniques¹⁸ could be applied, but an algorithmic investigation of optimality is beyond the scope of this study. Interestingly (p, q) space is characterized by a non-Gaussian distribution that does not contain explicit data clusters. Nevertheless, D-SEG provides a discrete mapping of this space dependent on local voxel density generating an intuitive separation of isotropic and anisotropic diffusion.

D-SEG provides reproducible segmentation of GM, WM, and CSF. Although D-SEG does not define exclusive segments for each tissue type, it provides a spectrum of diffusion properties supporting previous findings of similar isotropic diffusivity in GM and WM, and heterogeneous anisotropic diffusion in WM.³⁵ In this study, CSF spaces exhibited high magnitudes of isotropic diffusion but also greater anisotropic diffusion than did GM. This effect was caused by the use of q to quantify anisotropic diffusion, which, unlike FA, is not scaled by the overall magnitude of diffusion within a voxel.¹⁷

We prospectively recruited 94 patients with histopathologically confirmed lesions occupying intracranial space over an 18-month period representing a cross section of brain tumors encountered in our neurosurgical practice. D-SEG analysis of these data show that combined tumor and edema VOIs determined by D-SEG correspond visually with the extent of tumor on standard MRI; however, their complex margins are indistinct on conventional MRI or within p and q maps. A range of region drawing techniques have been used to determine diffusion characteristics of tumors, such as from manually drawn lesion edges³⁶ or from within ROIs placed in specified brain regions.³⁷ These techniques are time-consuming and user dependent and are subjective interpretations of the tumor boundary.³⁸ In

contrast, D-SEG generates tissue type boundaries based on an objective clustering of the isotropic and anisotropic diffusivities in (p, q) space. Such segmentation may reflect underlying differences in tissue microstructure and potentially relevant pathological boundaries. However, partial volume effects may result in D-SEG boundaries that do not accurately represent the precise difference between pathological and healthy tissue, and further work is required to determine the histological ground truth of D-SEG boundaries.

Brain tumors are characterized by their heterogeneity in size, location, and extent of perilesional edema.³⁹ Limitations of previous brain tumor diffusion studies are twofold: (i) placement of ROIs significantly smaller than the lesion potentially excludes relevant diffusion information; (ii) computation of average information over whole-lesion ROIs obscures heterogeneous diffusion characteristics within the tumor. Spectral comparison using D-SEG overcomes these limitations by providing a pattern of diffusivity across the entire region of abnormal tissue.

D-SEG spectra differ among tumor types in both their constituent segment numbers and their proportional contribution to the VOI. Spectra are consistent within the tumor type, confirmed by small standard errors for segments despite variability in size, location, natural history, and, in the case of metastases, cellular origin of each lesion. Possible reasons for differences in diffusion characteristics between tumor types include presence of necrotic or cystic regions or volumetric proportion of tumor and edema, solid tumor microstructure, and pathophysiology of perilesional edema.

Malignant tumors are characterized by rapid growth and neovascularity. When tumor rate of growth exceeds its blood supply, cell death and regional necrosis result.⁴⁰ The loss of cellular structure and boundaries to diffusion results in higher isotropic diffusion⁴¹ and is observed in glioblastoma D-SEG spectra. Tumor cysts may result from necrotic degeneration, central hemorrhage, liquefaction, entrapment of CSF, and plasma fluid leaking from a disrupted blood-brain barrier.⁴² Cysts have high isotropic diffusivity in the D-SEG spectra, reflecting the fluid nature of these regions. Glioblastoma cysts exhibit lower isotropic diffusivity than normal CSF spaces, potentially reflecting their proteinaceous constituents.

The solid component of tumors consists of disorganized pleomorphic, hypercellular cells with hyperchromatic nuclei, lacking the organized structure of nascent neural tissue.⁴³ In common with previous studies, D-SEG spectra indicate that isotropic diffusion within the solid tumor contributes to differentiating among tumor types.^{41,44,45} In particular, differences in cell density of the solid tumor may be responsible for observed spectral differences in the proportion of isotropic and anisotropic segments among tumor types. Our results confirm that isotropic diffusion is smaller in glioblastoma than in low-grade glioma, agreeing with previous studies,^{37,46,47} and contrasts the high cellularity of glioblastoma with cellularity that is only moderately increased compared with normal brain in low-grade glioma. D-SEG spectra confirm a lower isotropic diffusion within the solid component of metastases than glioblastoma, agreeing with previous studies.^{7,36} This contrasts the densely packed and restricted diffusion within secondary tumors with the irregular cellular arrangement of microscopic necrosis in glioblastoma. Meningioma D-SEG spectra are markedly

different from the other tumor types. The solid tumor component has the lowest isotropic diffusion and an anisotropic diffusion component that likely reflects interdigitating cellular processes, tight intercellular junctions, and formation of fascicular and lobular tissue in association with whorls and psammoma bodies.

D-SEG spectra differ in segments containing perilesional edema. Tumors with vasogenic edema, such as metastases and meningioma, comprise a greater proportion of segments with higher isotropic diffusion than infiltrative cellular edema in glioblastoma. These findings agree with previous studies and reflect the differences in pathophysiology of the edema.^{36,46}

Due to the ability of D-SEG to capture differences among tumors, it provides exceptional accuracy in tackling clinically relevant diagnostic scenarios, including differentiating glioma grade and discriminating between isolated metastases and glioblastoma. Although D-SEG accurately distinguishes metastases and meningioma, this has limited clinical use except for differentiating durally based metastatic deposits from benign meningioma.

D-SEG delineated a clear boundary between tumor and normal-appearing brain tissue for all except a small number of meningioma cases. In these cases the meningioma displayed anisotropic diffusion properties similar to healthy WM. Here it was necessary to manually draw lesion boundaries for the VOI guided by conventional postcontrast T1-weighted images. A further limitation is that diffusion properties identified by D-SEG are not exclusively representative of healthy or pathological tissue types due to tissue partial volume effects, effects of noise, and certain tumor tissue types sharing similar diffusivities to healthy brain tissue. The use of D-SEG spectra overcomes these problems by providing proportions of segments within VOIs. The 94 brain tumor cases acquired in this study represent the largest reported cohort of tumor DTI data. Further evaluation of the role of D-SEG in diagnosis requires comparing the accuracy of this method with the accuracy of reporting of conventional imaging, as well as testing with other tumor types and grades and a range of different metastases, as the site of primary disease and thus cell lineage may influence microstructure and thus tumor p - q diffusion characteristics.

Conclusion

Advances in imaging of newly identified lesions occupying intracranial space have not eliminated the requirement for histopathological “tissue” diagnosis in the majority of cases. With an increasing elderly population, improved survival in systemic malignancy, and increased detection of lesions (potentially incidentally) at an early stage, there exists a need for accurate and reproducible noninvasive diagnostic tools. In this study, we present a technique capable of classifying brain tumors using biomarkers obtained from DTI with an accuracy of 94.7%. The potential roles for D-SEG include: (i) delineation of lesion margins for optimal surgical resection or radiotherapy treatment, (ii) serial volumetric analysis to monitor changes in low-grade glioma over time or evaluate response to oncotherapy, and (iii) regional assessment of biomarkers for diagnosis or surveillance. Further studies are required to replicate

these results and determine the additional utility of D-SEG in these and other clinical scenarios.

Funding

This work was supported by Cancer Research UK, grant nos. C8807/A3870 and C1459/A13303; the EU, grant no. LSHC-CT-2004-503094 (eTUMOUR); and T.L.J. acknowledges a Royal College of Surgeons of England Research Fellowship.

Acknowledgments

We thank Chris Clark, Dominick McIntyre, and Alan Wright for their help with the MR imaging.

Conflict of interest statement. We have no conflicts of interest to declare.

References

1. Darefsky AS, King JT, Dubrow R. Adult glioblastoma multiforme survival in the temozolomide era: a population-based analysis of Surveillance, Epidemiology, and End Results registries. *Cancer*. 2012;118(8):2163–2172.
2. Koay E, Sulman EP. Management of brain metastasis: past lessons, modern management, and future considerations. *Curr Oncol Rep*. 2012;14(1):70–78.
3. Stupp R, Mason WP, van den Bent MJ, et al. Radiotherapy plus concomitant and adjuvant temozolomide for glioblastoma. *N Engl J Med*. 2005;352(10):987–996.
4. Stummer W, Pichlmeier U, Meinel T, et al. Fluorescence-guided surgery with 5-aminolevulinic acid for resection of malignant glioma: a randomised controlled multicentre phase III trial. *Lancet Oncol*. 2006;7(5):392–401.
5. McGirt MJ, Woodworth GF, Coon AL, et al. Independent predictors of morbidity after image-guided stereotactic brain biopsy: a risk assessment of 270 cases. *J Neurosurg*. 2005;102(5):897–901.
6. Kondziolka D, Lunsford LD, Martinez AJ. Unreliability of contemporary neurodiagnostic imaging in evaluating suspected adult supratentorial (low-grade) astrocytoma. *J Neurosurg*. 1993;79(4):533–536.
7. Wang S, Kim S, Chawla S, et al. Differentiation between glioblastomas and solitary brain metastases using diffusion tensor imaging. *Neuroimage*. 2009;44(3):653–660.
8. Tagle P, Villanueva P, Torrealba GHI. Intracranial metastasis or meningioma? *Surg Neurol*. 2002;58(3–4):241–245.
9. Basser PJ. Inferring microstructural features and the physiological state of tissues from diffusion-weighted images. *NMR Biomed*. 1995;8(7–8):333–344.
10. Basser PJ, Mattiello J, LeBihan D. Estimation of the effective self-diffusion tensor from the NMR spin echo. *J Magn Reson B*. 1994;103(3):247–254.
11. Pierpaoli C, Basser PJ. Toward a quantitative assessment of diffusion anisotropy. *Magn Reson Med*. 1996;36(6):893–906.
12. Stadlbauer A, Ganslandt O, Buslei R, et al. Gliomas: histopathologic evaluation of changes in directionality and magnitude of water diffusion at diffusion-tensor MR imaging. *Radiology*. 2006;240(3):803–810.

13. Beppu T, Inoue T, Shibata Y, et al. Fractional anisotropy value by diffusion tensor magnetic resonance imaging as a predictor of cell density and proliferation activity of glioblastomas. *Surg Neurol.* 2005;63(1):56–61.
14. Lu S, Ahn D, Johnson G, et al. Peritumoral diffusion tensor imaging of high-grade gliomas and metastatic brain tumors. *AJNR Am J Neuroradiol.* 2003;24(5):937–941.
15. Provenzale JM, Mcgraw P, Mhatre P, et al. Peritumoral brain regions in gliomas and meningiomas: investigation with isotropic imaging and diffusion-tensor. *Radiology.* 2004;232(2):451–460.
16. Tsuchiya K, Fujikawa A, Nakajima M, et al. Differentiation between solitary brain metastasis and high-grade glioma by diffusion tensor imaging. *Br J Radiol.* 2005;78(930):533–537.
17. Peña A, Green HAL, Carpenter TA, et al. Enhanced visualization and quantification of magnetic resonance diffusion tensor imaging using the p:q tensor decomposition. *Br J Radiol.* 2006;79(938):101–109.
18. Gordillo N, Montseny E, Sobrevilla P. State of the art survey on MRI brain tumor segmentation. *Magn Reson Imaging.* 2013;31(8):1426–1438.
19. Fletcher-Heath LM, Hall LO, Goldgof DB, et al. Automatic segmentation of non-enhancing brain tumors in magnetic resonance images. *Artif Intell Med.* 2001;21(1–3):43–63.
20. Clark MC, Hall LO, Goldgof DB, et al. Automatic tumor segmentation using knowledge-based techniques. *IEEE Trans Med Imaging.* 1998;17(2):187–201.
21. Liu J, Udupa JK, Odhner D, et al. A system for brain tumor volume estimation via MR imaging and fuzzy connectedness. *Comput Med Imaging Graph.* 2005;29(1):21–34.
22. Clarke LP, Velthuizen RP, Phuphanich S, et al. MRI: stability of three supervised segmentation techniques. *Magn Reson.* 1993;11(0730–725X (Print)):95–106.
23. Vijayakumar C, Damayanti G, Pant R, et al. Segmentation and grading of brain tumors on apparent diffusion coefficient images using self-organizing maps. *Comput Med Imaging Graph.* 2007;31(7):473–484.
24. Simon D, Fritzsche KH, Thieke C, et al. Diffusion-weighted imaging-based probabilistic segmentation of high- and low-proliferative areas in high-grade gliomas. *Cancer Imaging.* 2012;12:89–99.
25. MacQueen JB. Kmeans Some methods for classification and analysis of multivariate observations. *5th Berkeley Symp Math Stat Probab 1967.* 1967;1:281–297.
26. Nanetti L, Cerliani L, Gazzola V, et al. Group analyses of connectivity-based cortical parcellation using repeated k-means clustering. *Neuroimage.* 2009;47(4):1666–1677.
27. Ashburner J, Friston KJ. Unified segmentation. *Neuroimage.* 2005;26(3):839–851.
28. Aurenhammer F. Voronoi diagrams. *ACM Comput Surv.* 1991;23(3):345–405.
29. Rorden C, Brett M. Stereotaxic display of brain lesions. *Behav Neurol.* 2000;12(4):191–200.
30. Cristianini N, Shawe-Taylor J. *An Introduction to Support Vector Machines and Other Kernel-based Learning Methods.* Cambridge: Cambridge University Press; 2000.
31. Murphy K. *Machine Learning: a Probabilistic Perspective.* Cambridge, MA: MIT Press; 2012.
32. Pfefferbaum A, Adalsteinsson E, Sullivan EV. Replicability of diffusion tensor imaging measurements of fractional anisotropy and trace in brain. *J Magn Reson Imaging.* 2003;18(4):427–433.
33. Vollmar C, O'Muircheartaigh J, Barker GJ, et al. Identical, but not the same: intra-site and inter-site reproducibility of fractional anisotropy measures on two 3.0T scanners. *Neuroimage.* 2010;51(4):1384–1394.
34. Bonekamp D, Nagae LM, Degaonkar M, et al. Diffusion tensor imaging in children and adolescents: reproducibility, hemispheric, and age-related differences. *Neuroimage.* 2007;34(2):733–742.
35. Pierpaoli C, Jezzard P, Basser PJ, et al. Diffusion tensor MR imaging of the human brain. *Radiology.* 1996;201(3):637–648.
36. Byrnes TJD, Barrick TR, Bell BA, et al. Diffusion tensor imaging discriminates between glioblastoma and cerebral metastases in vivo. *NMR Biomed.* 2011;24(1):54–60.
37. Price SJ, Peña A, Burnet NG, et al. Tissue signature characterisation of diffusion tensor abnormalities in cerebral gliomas. *Eur Radiol.* 2004;14(10):1909–1917.
38. Kaus MR, Warfield SK, Nabavi A, et al. Automated segmentation of MR images of brain tumors. *Radiology.* 2001;218(2):586–591.
39. Kleihues P, Louis DN, Scheithauer BW, et al. The WHO classification of tumors of the nervous system. *J Neuropathol Exp Neurol.* 2002;61(3):215–225.
40. Raza SM, Lang FF, Aggarwal BB, et al. Necrosis and glioblastoma: a friend or a foe? A review and a hypothesis. *Neurosurgery.* 2002;51(1):2–12.
41. Krabbe K, Gideon P, Wagn P, et al. MR diffusion imaging of human intracranial tumours. *Neuroradiology.* 1997;39(7):483–489.
42. Poisson M, Philippon J, van Effenterre R, et al. Cerebral pseudocysts following chemotherapy of glioblastomas. *Acta Neurochir (Wien).* 1977;39(3–4):143–149.
43. Louis DN, Ohgaki H, Wiestler OD, et al. The 2007 WHO classification of tumours of the central nervous system. *Acta Neuropathol.* 2007;114(2):97–109.
44. Bulakbasi N, Kocaoglu M, Ors F, et al. Combination of single-voxel proton MR spectroscopy and apparent diffusion coefficient calculation in the evaluation of common brain tumors. *AJNR Am J Neuroradiol.* 2003;24(2):225–233.
45. Kono K, Inoue Y, Nakayama K, et al. The role of diffusion-weighted imaging in patients with brain tumors. *AJNR Am J Neuroradiol.* 2001;22(6):1081–1088.
46. Lu S, Ahn D, Johnson G, et al. Diffusion-tensor MR imaging of intracranial neoplasia and associated peritumoral edema: introduction of the tumor infiltration index. *Radiology.* 2004;232(1):221–228.
47. Inoue T, Ogasawara K, Beppu T, et al. Diffusion tensor imaging for preoperative evaluation of tumor grade in gliomas. *Clin Neurol Neurosurg.* 2005;107(3):174–180.
48. Lu S, Ahn D, Johnson G, Cha S. Peritumoral diffusion tensor imaging of high-grade gliomas and metastatic brain tumours. *AJNR Am J Neuroradiol.* 2003;24(5):937–941.